Flow, Turbulence and Combustion **67:** 235–265, 2001.

Linear Stability Analysis of a Viscous Liquid Sheet in a High-Speed Viscous Gas

GUILLERMO HAUKE[1], CÉSAR DOPAZO[1,2], ANTONIO LOZANO[2], FÉLIX BARRERAS[2] and AREZKY H. HERNÁNDEZ[3]
[1]*Area de Mecánica de Fluidos, Centro Politécnico Superior, Universidad de Zaragoza, C/Maria de Luna 3, 50015 Zaragoza, Spain*
[2]*LITEC/CSIC, C/Maria de Luna 3, 50015 Zaragoza, Spain*
[3]*Facultad de Ciencias Físicas, Universidad de La Habana, La Habana, Cuba*

Received 18 May 2001; accepted in revised form 3 December 2001

Abstract. Air-assisted atomizers in which a thin liquid sheet is deformed under the action of a high-speed air flow are extensively used in industrial applications, e.g., in aircraft turbojet injectors. Primary atomization in these devices is a consequence of the onset and growth of instabilities on the air/liquid interfaces. To better understand this process, a temporal linear instability analysis is applied to a thin planar liquid sheet flowing between two semi-infinite streams of a high-speed viscous gas. This study includes the full viscous effects both in the liquid and gas basic states and perturbations. The relevant dimensionless groups entering the non-dimensional Orr–Sommerfeld equations and boundary conditions are the liquid and gas stream Reynolds numbers, the gas to liquid momentum flux ratio, the gas/liquid velocity ratio, the Weber number and the equivalent gas boundary layer to liquid sheet thickness ratio. Growth rates and temporal frequencies as a function of the wavenumber, varying the different dimensionless parameters are presented, together with neutral stability curves. From the results of this parametric study it is concluded that when the physical properties of gas and liquid are fixed, the momentum flux ratio is especially relevant to determine the instability conditions. It is also observed that the gas boundary layer thickness strongly influences the wave propagation, and acts by damping sheet oscillation frequency and growth. This is especially important because viscosity in the basic gas velocity profile has always been ignored in instability analysis applied to the geometry under study.

Key words: gas-liquid interphases, instabilities, linear instability analysis.

1. Introduction

Although spray flows are present in many daily applications, the basic physical mechanisms underlying the atomization processes are still not completely understood. Two typical designs are pressure atomizers, where a pressurized liquid stream exits into a quiescent atmosphere, and twin-fluid atomizers, where an interacting gas/vapor coflow induces the liquid breakup. To this second group belongs the so-called air-assisted or "air-blast" type, in which the air stream flows at a much higher speed surrounding the liquid. In order to accelerate the atomization process, the liquid stream in atomizing nozzles is injected as a sheet, which in many cases is

axisymmetric. However, for basic studies of primary atomization, the large aspect ratio planar liquid sheet is almost becoming a canonical flow because of its relative simplicity, in particular, for flow visualization and for numerical simulation.

The first systematic studies on the breakup of a liquid sheet into droplets to generate a spray date back to the past century with the experiments performed by Savart [31] in 1833. The sheet was formed by impinging a water jet onto a disk, forming a water bell similar to those studied by Taylor [35] a century later. Over the last five decades, experimental studies, mostly based on visual observations, have been conducted together with theoretical analysis. Restricting this review to numerical simulations, linear stability methods were first applied to a planar sheet geometry by Squire [34], York et al. [42], Hagerty and Shea [15] and Taylor [36]. The case of thin liquid sheets in quiescent air was treated considering potential flows. Sinuous (antisymmetric) and varicose (dilatational or symmetric) waves were predicted. It is noteworthy that the two wave types were experimentally observed in the research of Hagerty and Shea, forcing initial perturbations by oscillating the nozzle tip.

Numerous papers by Dombrowski and coworkers have dealt with experimental and theoretical investigations on short aspect ratio nozzles generating the so called water fans [10, 12]. Dombrowski and Johns [11] assumed a viscous liquid sheet in a quiescent inviscid gas; from a balance of forces acting upon a fluid element at the interface, they concluded that liquid viscosity adds a dependence of the growth rate not only on wavenumber but also on sheet thickness. Crapper et al. [7] unsuccessfully tried to compare their inviscid results with experimental data. In all these studies, boundary conditions at the gas/liquid interfaces corresponded to those of a shear-free surface. Under this simplification, the tangential stress of the liquid was set equal to zero and the dynamic effect of the gas on the liquid sheet was, thus, completely ignored. Aiming at treating a more realistic configuration, Crapper et al. [8] considered viscosity in both fluids and parabolic velocity profiles for the basic liquid flow, with no free stream gas velocity; moreover, the equations were solved approximating the liquid profile to a constant velocity. The frequency instability range was widened due to viscosity and the oscillation was found to be independent of the liquid viscosity. Lin et al. [21] found that a viscous ambient gas dragged along by the liquid motion tended to destabilize the sheet and to shorten both sinuous and varicose mode wavelengths. Li and Tankin [22] treated a viscous liquid sheet in an inviscid gas, based on the perturbation, and conducted a temporal growth study, obtaining a viscosity-enhanced instability coincident with that predicted by Crapper et al. Rangel and Sirignano [29] performed linear and non-linear stability analyses of an inviscid liquid sheet in a moving inviscid gas. Ibrahim [17] analyzed the spatial growth of a perturbation for the configuration of Li and Tankin, obtaining different results. These studies were extended to a three-dimensional geometry in [19].

When the results obtained for quiescent air cases are directly applied to predict air-blast configurations, comparisons with experimental data fail dramatically, be-

cause the sheet oscillation has been proved to be mainly controlled by the air flow dynamics [1]. Consequently, the air effects cannot be neglected.

The problem considering high-speed air streams has been analyzed by Yang [39], Ibrahim [18] and Cousin and Dumouchel [6]. None of them, however, has included air viscosity in the perturbation equations.

Teng et al. [37] investigated the stability of a thin viscous liquid sheet flowing into a quiescent viscous gas confined between two parallel walls. In this study, the fully developed velocity profiles and the perturbations vanish at the solid walls. Absolute instability did occur when the Weber number was approximately one. Although this analysis includes the viscous effects thoroughly, the physical configuration of this problem corresponds to a pressure atomizer rather than to an air-assisted one. Therefore, the instability mechanisms triggered by the high-speed gas dynamics coupled to the liquid sheet motion are absent.

Yiantsios and Higgins [40], Smith [32] and Tilley et al. [38] have described the instability mechanisms induced by viscosity and density differences in channel flows. Interfacial shear plays a crucial role in other related problems, such as wind-generated waves [3, 5, 27] and wind-sheared liquid films in contact with solid walls [9, 26, 33, 41].

This study is aimed at improving the understanding of the interaction at the gas/liquid interfaces among a thin liquid sheet and two gas coflows, in the region very near the injection nozzle exit. To this end, an improved mathematical formulation has been developed considering viscous forces in the air and liquid basic flows, as well as in their perturbations. In doing so, the interface boundary conditions better reflect the real situation, including pressure and viscous stresses in balance with surface tension forces. Velocity profiles at a given downstream location have been approximated by parabolic ones. The dependence with the x-coordinate in the solution has not been considered for two main reasons. First, once the instability has been triggered the frequency remains constant, as has been shown experimentally [25], and there is no need to recalculate the oscillation frequency at different x-stations. Consequently, this study will not be able to predict the actual physical shape of the interphase once the non-linear effects become apparent. However, the instability triggering mechanisms should be properly described. The second reason why the x-dependence has been ignored is the extraordinary complexity of performing a full spatially and temporally evolving instability analysis, which exceeds the present framework. The mathematical formulation is analyzed in Section 2 of the paper. Section 3 is devoted to explain the numerical method used to solve the dispersion relation. The main results are presented in Section 4. Conclusions are drawn in Section 5.

2. Mathematical Formulation

The linear stability analysis of a two-dimensional sheet of constant thickness, $2h$, of a viscous liquid sandwiched between two identical semi-infinite viscous gas

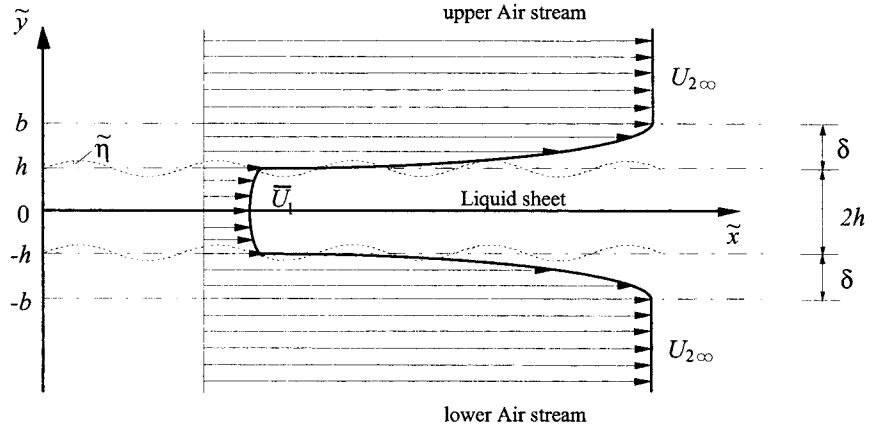

Figure 1. Sketch of the flow configuration considered in the study.

streams is considered. High Reynolds-number gas flows are assumed, thus characterizing them by the speed $U_{2\infty}$ far from the liquid sheet centerline and by the gaseous boundary layer local thicknesses, δ. The gas streams interact with the liquid sheet through pressure and viscous stresses at the interfaces $y = \pm h$ (see Figure 1). Liquid and gas phases are identified by subindices 1 and 2, respectively.

2.1. BASIC FLOWS

At a particular x station of the boundary layers (the nozzle exit), the velocity profiles are approximated by quadratic functions of y; at the same time, since within the boundary layer the transverse velocity component is much smaller than the downstream one, both liquid and gas flows are assumed parallel. The error involved in this approximation is of the order of the relative boundary layer thickness, i.e. $\delta/x \approx 1/\sqrt{\mathrm{Re}_x}$, which for large Reynolds numbers is small. Furthermore, Gaster [13] and Bertolloti et al. [4] show that the effects of non-parallelism are weak and not responsible for discrepancies between theory and experiments. In any case, the definite instability frequency is set at the nozzle exit and spread by convection downstream [25], making the first sections of the flow essential to the onset and development of the overall instability.

An alternative to define the basic unperturbed flows could have been to solve two Blasius type equations (for the gas-side and liquid-side boundary layers) coupled through the interface velocity. The numerical solution for the basic flows could then be used to conduct the perturbation study. However, the difference between a parabolic and a Blasius velocity profile is not significant for the physical mechanisms controlling the instability onset, whereas the parabolic profiles ease the analytical treatment of the equations.

The unknown coefficients of the assumed basic state velocity profiles are calculated by forcing them to satisfy certain constraints, in a manner similar to that of

the von Kármán–Pohlhausen method for integral boundary layer solutions. This is only considered a first attempt to understand the basic mechanisms of this problem and it is basically expected, for the reasons already stated, that the proposed local approximation does not alter the underlying physical processes. On the other hand, direct numerical simulations of these flows near the nozzle exit tend to indicate that, under conditions for which the linear instability analysis may be valid, the liquid sheet thickness remains approximately constant [23].

The unperturbed velocity profiles are therefore approximated by

$$\hat{U}_1(\tilde{y}) = a_0 + a_2\tilde{y}^2, \quad -h \le \tilde{y} \le h, \tag{1}$$

$$\hat{U}_2(\tilde{y}) = b_0 + b_1\left(\frac{\tilde{y}-h}{\delta}\right) + b_2\left(\frac{\tilde{y}-h}{\delta}\right)^2, \quad h \le \tilde{y} \le h+\delta, \tag{2}$$

$$\hat{U}_2(\tilde{y}) = b_0 - b_1\left(\frac{\tilde{y}+h}{\delta}\right) + b_2\left(\frac{\tilde{y}+h}{\delta}\right)^2, \quad -(h+\delta) \le \tilde{y} \le -h, \tag{3}$$

with $h \le \tilde{y} \le h+\delta$ for the upper gas stream and $-(h+\delta) \le \tilde{y} \le -h$ for the lower gas stream. In order to determine the coefficients a_i and b_i ($i = 0, 1, 2$), the following five constraints are imposed:

(i) The volumetric liquid flow rate or, equivalently, the liquid mean velocity, $\bar{U}_1$, is given.
(ii) The air and liquid velocities at the unperturbed interfaces, $y = \pm h$, are equal.
(iii) The tangential viscous stresses balance at the unperturbed interface.
(iv) The air velocities at the boundary layer edges, $\tilde{y} = \pm(h+\delta)$, equal $U_{2\infty}$.
(v) The air velocity gradients at the boundary layer edges vanish.

Solving the five algebraic equations yields

$$\begin{aligned}
a_0 &= \bar{U}_1\left(1 + \frac{1}{3}\frac{\mu_r}{\Delta}\right) - U_{2\infty}\frac{1}{3}\frac{\mu_r}{\Delta},\\
a_2 &= \frac{U_{2\infty} - \bar{U}_1}{h^2}\frac{\mu_r}{\Delta},\\
b_0 &= U_{2\infty}\left(1 - \frac{l}{\Delta}\right) + \bar{U}_1\frac{l}{\Delta},\\
b_1 &= \left(U_{2\infty} - \bar{U}_1\right)\frac{2l}{\Delta},\\
b_2 &= -\left(U_{2\infty} - \bar{U}_1\right)\frac{l}{\Delta},
\end{aligned} \tag{4}$$

where $\mu_r = \mu_2/\mu_1$ is the gas/liquid viscosity ratio, $l = \delta/h$ is the ratio of the gas boundary layer thickness to the liquid sheet half thickness and $\Delta = (2/3)\mu_r + l$.

The parallel flow approximation for the basic flows implies a balance between pressure and viscous forces; the assumed quadratic profiles lead to constant pressure gradients of opposite sign in the gas and the liquid flows, namely, linear downstream pressure variations with a positive slope for the liquid and a negative slope for the gas. This might lead to inconsistencies due to the pressure imbalance in the two fluids. However, due to the smallness of the pressure gradients, for flows at atmospheric pressures and for the region very near the nozzle tip, the pressure changes are extremely small (less that 0.10%).

On the other hand two coupled boundary layer type integral equations can be easily obtained for the liquid sheet and the gas boundary layer, respectively; the sheet thickness and the boundary layer thickness are considered functions of x. The approximate velocity profiles can then be inserted into the integral equations to calculate momentum thickness and friction coefficients. As a consequence, the approximate evolutions of $h(x)$ and $\delta(x)$ for a consistent boundary layer type of approach can be obtained. However, this alternative is of no relevance to the local instability approximation adopted here.

2.2. PERTURBATION FLOWS

The perturbation flow stream functions, $\Psi_\alpha(\tilde{x}, \tilde{y}, t)$, are expressed as a normal mode decomposition, namely,

$$\Psi_\alpha(\tilde{x}, \tilde{y}, t) = \tilde{\phi}_\alpha(\tilde{y})\, \mathrm{e}^{i\tilde{k}\tilde{x}+\tilde{\omega}t}, \tag{5}$$

where $\tilde{\phi}_\alpha(\tilde{y})$ are the amplitudes of the normal mode disturbances, $\tilde{\omega}$ is the complex frequency and $\tilde{k}$ is the real wavenumber of the perturbation. By definition, the perturbation velocity field is

$$\begin{aligned} u_\alpha &= \frac{\partial \Psi_\alpha(\tilde{x}, \tilde{y}, t)}{\partial \tilde{y}}, \\ v_\alpha &= -\frac{\partial \Psi_\alpha(\tilde{x}, \tilde{y}, t)}{\partial \tilde{x}}. \end{aligned} \tag{6}$$

The linear stability of the basic state, given by (1–3), with respect to the normal mode two-dimensional perturbations is governed by two coupled Orr-Sommerfeld equations

$$\begin{aligned} \tilde{\phi}_\alpha^{iv}(\tilde{y}) &- \frac{i\tilde{k}}{\nu_\alpha}\left[\frac{\tilde{\omega}}{i\tilde{k}} + \hat{U}_\alpha(\tilde{y}) + \frac{2\nu_\alpha\tilde{k}^2}{i\tilde{k}}\right]\tilde{\phi}_\alpha''(\tilde{y}) \\ &+ \frac{i\tilde{k}}{\nu_\alpha}\left\{\tilde{k}^2\left[\frac{\tilde{\omega}}{i\tilde{k}} + \hat{U}_\alpha(\tilde{y}) + \frac{\nu_\alpha\tilde{k}^2}{i\tilde{k}}\right] + \hat{U}_\alpha''(\tilde{y})\right\}\tilde{\phi}_\alpha(\tilde{y}) = 0, \end{aligned} \tag{7}$$

where, as already stated, $\alpha = 1$ for the liquid and $\alpha = 2$ for the gases. The pressure and interfacial displacement modes are written as

$$[\tilde{p}_\alpha(\tilde{x}, \tilde{y}, t), \tilde{\zeta}(\tilde{x}, t)] = [\tilde{p}_\alpha(\tilde{y}), \tilde{\eta}_\pm]\, \mathrm{e}^{i\tilde{k}\tilde{x}+\tilde{\omega}t}, \tag{8}$$

where $\tilde{\zeta}_+(\tilde{x}, t)$ and $\tilde{\zeta}_-(\tilde{x}, t)$ are, respectively, the upper and lower interface displacements from the equilibrium position. For sinuous waves $\tilde{\zeta}_-(\tilde{x}, t) = \tilde{\zeta}_+(\tilde{x}, t)$ and for varicose waves $\tilde{\zeta}_-(\tilde{x}, t) = -\tilde{\zeta}_+(\tilde{x}, t)$.

The kinematic boundary conditions at the interfaces can be written as

$$i\tilde{k}\tilde{\phi}_\alpha(\pm h) + [\tilde{\omega} + i\tilde{k}\hat{U}_\alpha(\pm h)]\tilde{\eta}_\pm = 0 \quad \text{for } \alpha = 1, 2. \tag{9}$$

The boundary conditions at the interfaces $\tilde{y} = \pm h + \tilde{\zeta}_\pm(\tilde{x}, t)$ are linearized about $\tilde{y} = \pm h$ and only the first order perturbations are retained. The no-slip conditions at the interfaces result in

$$[\tilde{\phi}'_\alpha(\pm h) + \tilde{\eta}_\pm \hat{U}'_\alpha(\pm h)]_1^2 = 0, \tag{10}$$

$$[\tilde{\phi}_\alpha(\pm h)]_1^2 = 0. \tag{11}$$

The linearized equations for the tangential and normal stress balances are expressed as

$$[\mu_\alpha(\tilde{\phi}''_\alpha(\pm h) + \tilde{k}^2\tilde{\phi}_\alpha(\pm h) + \tilde{\eta}_\pm \hat{U}''_\alpha(\pm h))]_1^2 = 0, \tag{12}$$

$$\begin{aligned}[\mu_\alpha(\tilde{\phi}'''_\alpha(\pm h) - 3\tilde{k}^2\tilde{\phi}'_\alpha(\pm h)) - \rho_\alpha(\tilde{\omega} + i\tilde{k}\hat{U}_\alpha(\pm h))\tilde{\phi}'_\alpha(\pm h) \\ + i\tilde{k}\hat{U}'_\alpha(\pm h)\tilde{\phi}_\alpha(\pm h)]_1^2 = \mp i\tilde{k}^3\sigma\tilde{\eta}_\pm.\end{aligned} \tag{13}$$

To these boundary conditions, one should add vanishing perturbation velocity far from the centerline,

$$\begin{aligned}\tilde{\phi}_2(\pm\infty) &= 0, \\ \tilde{\phi}'_2(\pm\infty) &= 0.\end{aligned} \tag{14}$$

The choice of the dimensionless variables

$$\begin{aligned} y &= \frac{\tilde{y}}{h}, \quad \omega = \frac{\tilde{\omega}h}{\bar{U}_1}, \\ k &= \tilde{k}h, \quad \eta_\pm = \frac{\tilde{\eta}_\pm}{h}, \\ U_1(y) &= \frac{\hat{U}_1(\tilde{y})}{\bar{U}_1}, \quad \phi_1(y) = \frac{\tilde{\phi}_1(\tilde{y})}{\bar{U}_1 h}, \\ U_2(y) &= \frac{\hat{U}_2(\tilde{y})}{\bar{U}_{2\infty}}, \quad \phi_2(y) = \frac{\tilde{\phi}_2(\tilde{y})}{\bar{U}_{2\infty}\delta} \end{aligned} \tag{15}$$

transforms the liquid domain to $-1 \le y \le 1$, the upper gas domain to $1 \le y \le$

$1 + l$ and the lower gas domain to $-(1 + l) \leq y \leq -1$. The dimensionless Orr–Sommerfeld equations become

$$\frac{1}{\mathrm{Re}_1}\phi_1^{iv}(y) - \left[\omega + ikU_1(y) + \frac{2}{\mathrm{Re}_1}\right]\phi_1''(y) + \left[k^2\left(\omega + ikU_1(y) + \frac{k^2}{\mathrm{Re}_1}\right) + ikU_1''(y)\right]\phi_1(y) = 0, \tag{16}$$

$$\frac{l}{\mathrm{Re}_2}\phi_2^{iv}(y) - \left[\omega V_{12} + ikU_2(y) + \frac{2l}{\mathrm{Re}_2}\right]\phi_2''(y) + \left[k^2\left(\omega V_{12} + ikU_2(y) + \frac{k^2 l}{\mathrm{Re}_2}\right) + ikU_2''(y)\right]\phi_2(y) = 0. \tag{17}$$

The boundary conditions in dimensionless form are written as

$$ik\phi_1(\pm 1) + [\omega + ikU_1(\pm 1)]\eta_\pm = 0, \tag{18a}$$

$$V_{12}\phi_1'(\pm 1) - l\phi_2'(\pm 1) + [V_{12}U_1'(\pm 1) - U_2'(\pm 1)]\eta_\pm = 0, \tag{18b}$$

$$V_{12}\phi_1(\pm 1) - l\phi_2(\pm 1) = 0, \tag{18c}$$

$$\phi_1''(\pm 1) + k^2\phi_1(\pm 1) - M_{\mathrm{fr}}\frac{\mathrm{Re}_1}{\mathrm{Re}_2}l^2[\phi_2''(\pm 1) + k^2\phi_2(\pm 1)] + \left[U_1''(\pm 1) - M_{\mathrm{fr}}\frac{\mathrm{Re}_1}{\mathrm{Re}_2}\,l\,U_2''(\pm 1)\right]\eta_\pm = 0, \tag{18d}$$

$$-[\omega + ikU_1(\pm 1)]\phi_1'(\pm 1) + lM_{\mathrm{fr}}[\omega V_{12} + ikU_2(\pm 1)]\phi_2'(\pm 1) - \frac{3k^2}{\mathrm{Re}_1}\phi_1'(\pm 1) + 3\frac{l^2 M_{\mathrm{fr}}}{\mathrm{Re}_2}k^2\phi_2'(\pm 1) + ikU_1'(\pm 1)\phi_1(\pm 1) - ilM_{\mathrm{fr}}kU_2'(\pm 1)\phi_2(\pm 1) + \frac{1}{\mathrm{Re}_1}\phi_1'''(\pm 1) - \frac{l^2 M_{\mathrm{fr}}}{\mathrm{Re}_2}\phi_2'''(\pm 1) \mp \frac{ik^3}{\mathrm{We}}\eta_\pm = 0, \tag{18e}$$

$$\phi_2(\pm\infty) = 0, \tag{18f}$$

$$\phi_2'(\pm\infty) = 0, \tag{18g}$$

In the previous equations $\mathrm{Re}_1 = \bar{U}_1 h/\nu_1$ is the liquid sheet Reynolds number, $\mathrm{Re}_2 = U_{2\infty}\delta/\nu_2$ the gas stream Reynolds number, $M_{\mathrm{fr}} = \rho_2 U_{2\infty}^2/(\rho_1 \bar{U}_1^2)$

the gas/liquid momentum flux ratio and We $= \rho_1 \bar{U}_1^2 h/\sigma$ the Weber number. Apart from these four dimensionless groups, the ratio of the gas boundary layer thickness to the liquid sheet half thicknesses, $l = \delta/h$, and the velocity ratio $V_{12} = 1/V_{21} = \bar{U}_1/U_{2\infty}$ enter the solution.

Note that the boundary conditions (18f, 18g) are imposed at infinity. In order to reduce the computational domain to a finite size, the analytical solution in the outer, constant velocity domains, i.e.,

$$\phi(y) = \begin{cases} C\,\mathrm{e}^{ky}, & y > 0, \\ C\,\mathrm{e}^{-ky} & y < 0, \end{cases} \tag{19}$$

(C is a free constant) is matched to the computed solution at the outer edge of the gas boundary layer, $y = \pm(1 + l)$. Thus, the new boundary conditions are

$$\begin{aligned} &\phi_2((1 + l)) = C\,\mathrm{e}^{k(1+l)}, \\ &\phi_2(-(1 + l)) = C\,\mathrm{e}^{-k(1+l)}. \end{aligned} \tag{20}$$

In order to retain the linearity of the boundary conditions, in (19) only the inviscid part of the analytical solution has been considered. Therefore, to replace the two boundary conditions and to determine the constant C, three constraints are necessary, namely, continuity of downstream velocity, of transverse velocity and of normal stresses. Thus, (18f, 18g) are replaced by

$$\begin{aligned} &\phi_2'(\pm(1 + l)) \pm k\,\phi_2(\pm(1 + l)) = 0, \\ &\phi_2'''(\pm(1 + l)) \pm k^3\,\phi_2(\pm(1 + l)) = 0. \end{aligned} \tag{21}$$

These boundary conditions allow the investigation of the viscous instability in an infinite domain, including the high-speed air effects and the gas boundary layer thickness. The flow confined between two parallel walls, with the liquid sheet flowing into a quiescent gas and the perturbation vanishing at the walls has been treated by Teng et al. [37]. However, the present configuration is clearly different from the latter, both, from a physical standpoint and from their mathematical formulation.

3. Numerical Procedure

In order to solve the previous system of coupled Orr–Sommerfeld equations, the Tau–Galerkin projection method is employed. The solution space is expanded in Chebyshev polynomials, which are defined in the closed interval $[-1, 1]$. The procedure is illustrated in detail in [14, 28, 37].

Since there are two media, the computational domain was divided into three zones: one liquid domain surrounded by two gas domains. For the uniform semi-infinite gas zones, analytical solutions for the perturbation were derived and, then, used as boundary conditions for the gas boundary-layer regions.

Within each zone the spatial coordinates must be mapped to $[-1, 1]$. This has already been done for zone 1, where $-1 \leq y \leq 1$. The corresponding mappings

for the remaining zones are defined as $y \in [1, 1+l] \longrightarrow y_{2+} \in [1, -1]$, and $y \in [-(1+l), -1] \longrightarrow y_{2-} \in [1, -1]$ which are expressed by the following linear transformations

$$\begin{aligned} y &= 1 - \frac{1}{2}\, l\, (y_{2+} - 1), \\ y &= -1 - \frac{1}{2}\, l\, (y_{2-} + 1). \end{aligned} \tag{22}$$

After introducing the change of variables, the basic velocity profiles can be expressed as

$$\begin{aligned} U_1(y) &= \frac{1}{2} K_1 y^2 + B_1, \\ U_{2\pm}(y_{2\pm}) &= E y_{2\pm}^2 \pm F y_{2\pm} + H, \end{aligned} \tag{23}$$

where

$$\begin{aligned} K_1 &= 2\frac{a_2 h^2}{\bar{U}_1}, \\ B_1 &= \frac{a_0}{\bar{U}_1}, \\ E &= \frac{1}{U_{2\infty}}(\frac{1}{4} b_2), \\ F &= -\frac{1}{2U_{2\infty}}(b_1 + b_2), \\ H &= \frac{1}{U_{2\infty}}(b_0 + \frac{1}{2} b_1 + \frac{1}{4} b_2). \end{aligned} \tag{24}$$

The change of variables also affects the derivatives, which must be multiplied by the Jacobian of the transformation. That is, in medium 2, the nth derivative of ϕ_2 and U_2 is multiplied by $(-2/l)^n$.

The perturbation amplitudes are then expanded in series of Chebyshev polynomials,

$$\phi_1(y) = \sum_{n=0}^{N_1} a_n T_n(y), \quad -1 \le y \le 1, \tag{25a}$$

$$\phi_{2+}(y_{2+}) = \sum_{n=0}^{N_2} b_n T_n(y_{2+}), \quad -1 \le y_{2+} \le 1, \tag{25b}$$

$$\phi_{2-}(y_{2-}) = \sum_{n=0}^{N_2} d_n T_n(y_{2-}), \quad -1 \le y_{2-} \le 1. \tag{25c}$$

In medium 1, the odd and even modes decouple and any solution can be expressed as a linear combination of the odd and even solutions. The even mode (the symmetric solution, formed by functions with even powers of y, i.e. $a_{2n+1} = 0$) generates the *sinuous* mode. In this mode $\phi(y) = \phi(-y)$, $\zeta_+(x,t) = \zeta_-(x,t)$. The odd mode (the antisymmetric solution, formed by odd powers of y, i.e., $a_{2n} = 0$) generates the *varicose* mode. Here $\phi(y) = -\phi(-y)$ and $\zeta_+(x,t) = -\zeta_-(x,t)$. In the solution of ϕ_2 and ϕ_3, the even and odd powers do not decouple.

The sinuous mode is obtained by retaining the even expansion for ϕ_1 and the varicose mode, by retaining the odd terms in the expansion. Attention will focus on the sinuous mode since the varicose mode is not experimentally observed. The boundary conditions for the sinuous mode, at $y = y_{2+} = 1$, are

$$\sum_{n=0}^{N_1} ika_{2n} + [\omega + ikU_1(1)]\eta_+ = 0, \tag{26a}$$

$$\sum_{n=0}^{N_1} V_{12}(2n)^2 a_{2n} - \sum_{n=0}^{N_2} l\left(-\frac{2}{l}\right) n^2 b_n + \left[V_{12}U_1'(1) - \left(-\frac{2}{l}\right)U_{2+}'(1)\right]\eta_+ = 0, \tag{26b}$$

$$\sum_{n=0}^{N_1} V_{12}a_{2n} - \sum_{n=0}^{N_2} lb_n = 0, \tag{26c}$$

$$\sum_{n=0}^{N_1}\left[\frac{4n^2(4n^2-1)}{3} + k^2\right]a_{2n} - \sum_{n=0}^{N_2} M_{\mathrm{fr}}\frac{\mathrm{Re}_1}{\mathrm{Re}_2}l^2\left[\left(-\frac{2}{l}\right)^2\frac{n^2(n^2-1)}{3} + k^2\right]b_n + \left[U_1''(1) - M_{\mathrm{fr}}\frac{\mathrm{Re}_1}{\mathrm{Re}_2}\,l\left(-\frac{2}{l}\right)^2 U_{2+}''(1)\right]\eta_+ = 0, \tag{26d}$$

$$\sum_{n=0}^{N_1}\left[-\left(\frac{3k^2}{\mathrm{Re}_1} + ikU_1(1)\right)4n^2 + ikU_1'(1) + \frac{4n^2(4n^2-1)(4n^2-4)}{15\mathrm{Re}_1} - \omega\,4n^2\right]a_{2n}$$

$$+\sum_{n=0}^{N_2} l M_{\mathrm{fr}} \left[\left(\frac{3k^2 l}{\mathrm{Re}_2} + ikU_{2+}(1) \right) \left(-\frac{2}{l} \right) n^2 - ik \left(-\frac{2}{l} \right) U'_{2+}(1) \right.$$

$$\left. - \frac{n^2(n^2-1)(n^2-4)}{15} \frac{l}{\mathrm{Re}_2} \left(-\frac{2}{l} \right)^3 + \omega V_{12} \left(-\frac{2}{l} \right) n^2 \right] b_n$$

$$- \frac{ik^3}{\mathrm{We}} \eta_+ = 0. \tag{26e}$$

At $y_{2+} = -1$, the boundary conditions are

$$\sum_{n=0}^{N_2} \left(\left(-\frac{2}{l} \right) (-1)^{n+1} n^2 + k(-1)^n \right) b_n = 0, \tag{27a}$$

$$\sum_{n=0}^{N_2} \left(\left(-\frac{2}{l} \right)^3 \frac{(-1)^{n+3} n^2 (n^2-1)(n^2-4)}{15} + k^3 (-1)^n \right) b_n = 0. \tag{27b}$$

All the equations have been written taking into account that $T_n(\pm 1) = (\pm 1)^n$, $T'_n(\pm 1) = (\pm 1)^{n+1} n^2$, $T''_n(\pm 1) = (\pm 1)^{n+2} n^2 (n^2-1)/3$, $T'''_n(\pm 1) = (\pm 1)^{n+3} n^2 (n^2-1)(n^2-4)/15$.

The unknowns are the coefficients a_{2n} $(0 \le n \le N_1)$, b_n $(0 \le n \le N_2)$ and η. That is, $N_1 + N_2 + 3$ unknowns. In the Tau–Galerkin method, the boundary conditions are imposed as additional equations which replace the higher order projections. Thus, $0 \le n \le N_1 - 1$ equations are retained for the liquid domain and $0 \le n \le N_2 - 3$ for the gas domain; the 7 boundary conditions are added in order to close the system of equations.

All the computations where performed in double precision arithmetic. The computation of the generalized eigenvalue problem was solved with the LAPACK zgegv.f subroutine [20] which required the BLAS library. The computer code was checked against other published data. In particular,

(i) Stability of Poiseuille flow [28].
(ii) Temporal stability of stratified flow [30].
(iii) Stability of a liquid sheet in a quiescent gas [37].

An example of convergence of the eigenvalue of maximum amplification is shown in Table I. In this method, one should be aware of spurious diverging eigenvalues, which should not be taken into account.

4. Results

A temporal stability analysis has been performed; for a given wavenumber, k, the complex temporal frequency, ω, is found. Temporal growth appears for a positive

Table I. Example of convergence of the maximum amplification rate at a fixed wavenumber. $\rho_1 = 998.0$ kg/m^3, $\rho_2 = 1.21$ kg/m^3, $\mu_1 = 0.89e-3$ kg/ms, $\mu_2 = 0.018e-3$ kg/ms, $\sigma = 71.99e-3$ Pa m, $U_{2\infty} = 15$ m/s, $\bar{U}_1 = 1$ m/s, $h = 0.175$ mm, $\delta = 0.32$ mm, $k = 0.02$.

N_1	N_2	ω_r	ω_i
4	8	0.0633400524	–0.0365095214
8	16	0.0633355793	–0.0364495698
16	32	0.0633355780	–0.0364495705

real part, $\omega_r > 0$. The imaginary part of the temporal frequency, ω_i, corresponds to the wave oscillation frequency and can be related to the wave propagation speed, c, through $c = \omega_i / k$.

The selected values for the variables employed in the analysis, such as the boundary layer thicknesses and air and water mean velocities, have been chosen to reflect realistic situations of atomization processes or values of reported experiments. In particular, air boundary layer thickness has been estimated according to the expression for a flat plate laminar boundary layer at a distance of 6 mm.

In Figure 2, the non-dimensional growth rates are plotted as functions of the non-dimensional wavenumber for a 350 μm thick water sheet exiting at 5 m/s, with coflowing air moving at 15 m/s (dotted line) and 0.1 m/s (solid line). The higher air velocity would correspond to an air-assisted atomization whereas the lower value would be close to a pressure atomizer. The present computer code is capable of analyzing both situations. Although not shown in the figure, it is to be noted that a decrease in air velocity does not necessarily imply a decrease in growth rate; however, for an air-blasted configuration with air velocity amply exceeding the water speed, this is true. Incidentally, for a water velocity of 5 m/s, the same sheet thickness and a solid wall placed at $\pm(h + \delta)$, the physical configuration described by Teng et al. [37] is stable. This result may well indicate that the physics involved in the problem of Teng et al. is different from that in the present one due to the specific basic states and boundary conditions (wall confined flow in the former, and infinite free air stream in the latter).

Figure 2 is customary for the amplification rate curves; for small wavenumbers, the curves monotonically increase until a maximum is reached; the presence of a maximum is due to surface tension effects; otherwise, the curve is monotonically increasing. Above the maximum, the curve decreases until the coordinate axis is crossed. The observed inflection point (change of curvature) and long tail are due to viscous effects in the perturbation flow.

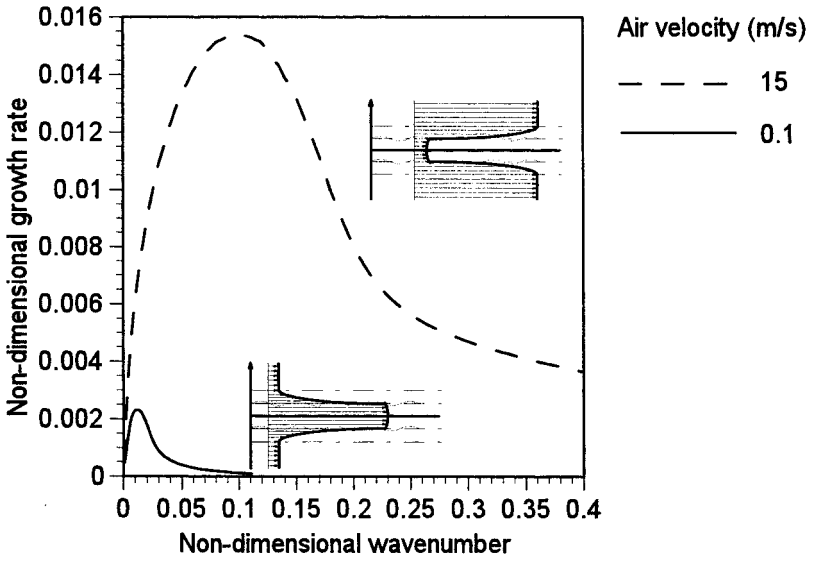

Figure 2. Dimensionless temporal growth rates obtained for two typical configurations for an air/water system. Air speed larger and smaller than liquid velocity. For the two cases, water velocity is kept constant at 5 m/s ($\mathrm{Re}_1 = 850$). For the higher air velocity (15 m/s) $\delta = 0.32$ mm and for the lower one (0.1 m/s) $\delta = 23.95$ mm.

4.1. VARIATION OF NON-DIMENSIONAL GROUPS

A parametric study of growth rates as a function of the wavenumber, varying the different dimensionless groups, is next presented. In order to independently and individually vary the relevant non-dimensional numbers (liquid and gas Reynolds numbers, momentum flux ratio, Weber number, gas boundary layer to liquid sheet thickness ratio and gas/liquid velocity ratio), the properties of the two fluids are first varied maintaining h, δ, $\bar{U}_1$ and $U_{2\infty}$ constant. A change of μ_1, then, yields a variation of Re_1, the other dimensionless groups remaining constant. Figure 3 is a plot of the temporal growth rate in terms of the wavenumber varying the liquid Reynolds number, Re_1. Increasing Re_1 leads to a wider range of unstable wavenumbers on the small wavelength side. It is to be noted that the wavelength at which the maximum growth rate occurs, as well as the value of the maximum growth rate, are extremely insensitive to these variations. In practical terms, this means that the characteristics of the spray are almost independent of the liquid viscosity. The imaginary part of the temporal frequency as a function of the wavenumber is presented in Figure 4. The slope of this curve yields the wave propagation speed, which is largely independent of the liquid Reynolds number. Below the inflection point, the propagation speed remains approximately equal to the liquid velocity (non-dimensional slope equal to one). Above the inflection point, the slope increases up to about two.

Changing only the gas dynamic viscosity, μ_2, causes a variation of Re_2, maintaining the five remaining dimensionless numbers constant. Figure 5 plots the

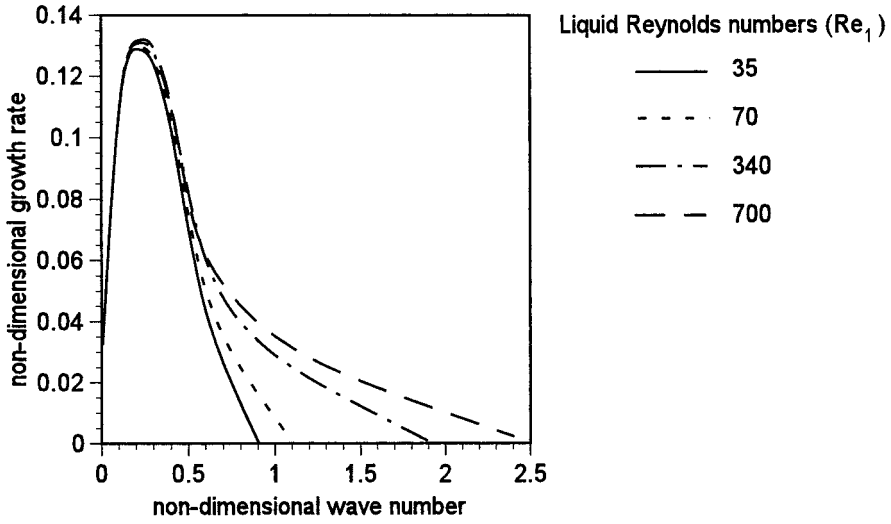

Figure 3. Dimensionless temporal growth rate as a function of non-dimensional wavenumber for $\mathrm{Re}_2 = 460$, We $= 9.7$, $M_{\mathrm{fr}} = 0.181$, $l = 1.4$, $V_{21} = 12.5$ and several liquid Reynolds numbers (Re_1).

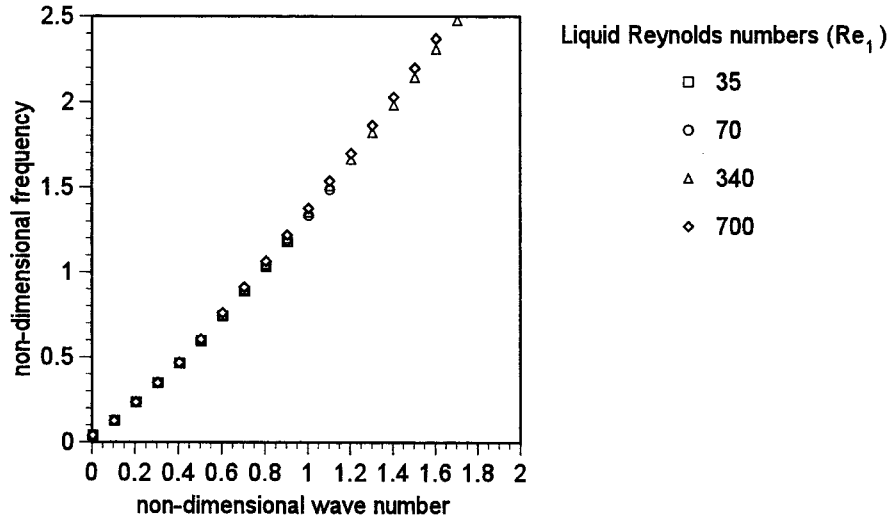

Figure 4. Dimensionless temporal frequency as a function of non-dimensional wavenumber for the same values of Re_2, We, M_{fr}, l and V_{21} as in Figure 1,and several liquid Reynolds numbers (Re_1).

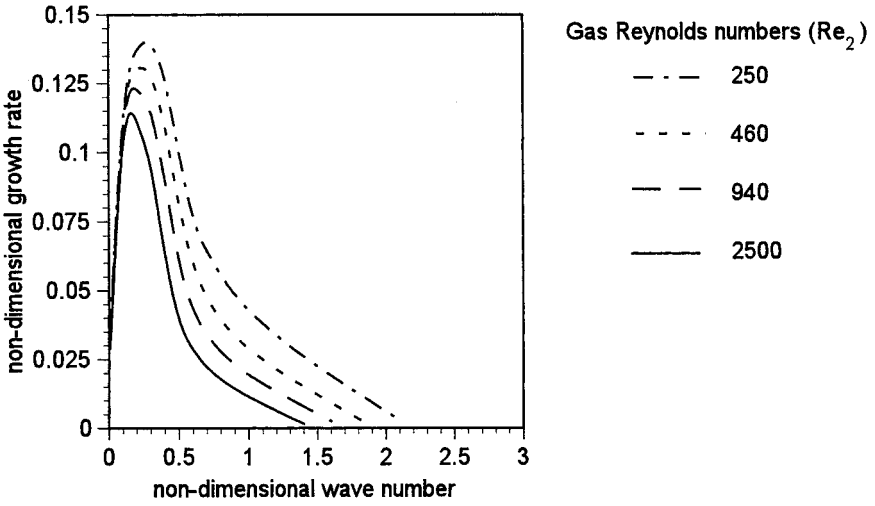

Figure 5. Dimensionless temporal growth rate as a function of non-dimensional wavenumber for $\mathrm{Re}_1 = 340$, We $= 9.7$, $M_{\mathrm{fr}} = 0.181$, $l = 1.4$, $V_{21} = 12.5$ and several gas Reynolds numbers (Re_2).

growth rate as a function of the wavenumber for several gas Reynolds numbers, Re_2; increasing Re_2 has a stabilizing effect on the sandwiched liquid sheet for small wavelengths. This influence is still moderate. The trends displayed in Figure 6 are almost identical to those of Figure 4, the non-dimensional frequency and wave speed being practically insensitive to changes in the gas Reynolds number.

Changing only the gas density, ρ_2, and its dynamic viscosity, μ_2, in such a manner that the gas kinematic viscosity remains constant, $\nu_2 = \mu_2/\rho_2$, yields a variation of M_{fr}, solely. Figure 7 indicates that an increase in the momentum flux ratio significantly enhances the growth rate, simultaneously destabilizing the small wavelengths. Larger momentum flux ratio numbers increase the wavenumbers where the maximum growth rate is attained. Viewing the momentum flux ratio as the relation between the gas and the liquid dynamic pressures, it is to be expected that larger gas pressures are potentially favorable for triggering the liquid sheet instability. Changes in the wave propagation speed with M_{fr} are apparent in Figures 8 and 9. Figure 9 shows the wave propagation speed at the wavenumber of maximum growth as a function of the M_{fr}. It can be seen that variations of M_{fr} have also a substantial effect on this parameter, which ranges from 1 for small M_{fr} to values in the neighborhood of 1.6 at large M_{fr} numbers.

Varying only the value of the surface tension, σ, changes the Weber number, We, while maintaining constant the five remaining dimensionless groups. Figure 10 depicts the temporal growth rate in terms of the wavenumber for several We; increasing surface tension has a stabilizing effect on the sheet oscillation as one could expect on intuitive grounds; the increment in σ reduces both the temporal growth rate and the range of unstable wavenumbers. Small wavelengths are prone

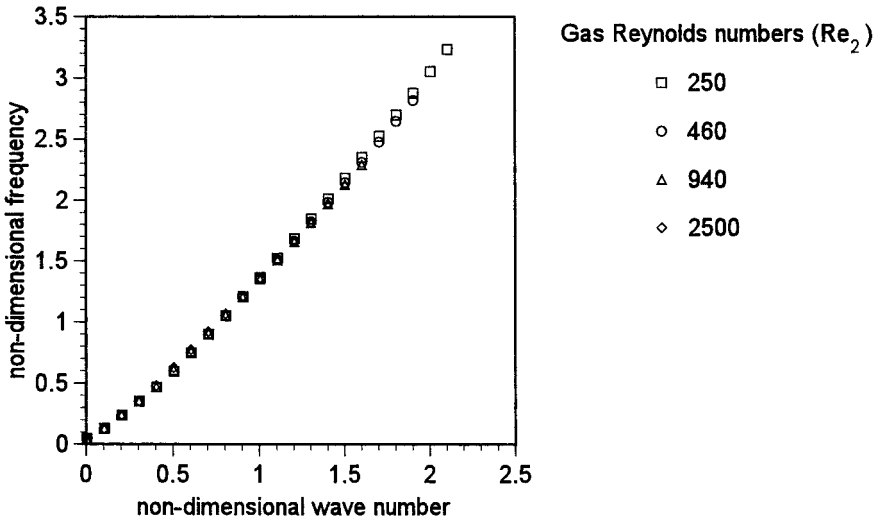

Figure 6. Dimensionless temporal frequency as a function of non-dimensional wavenumber for the same values Re_1, We, M_{fr}, l, V_{21} as in Figure 3, and several gas Reynolds numbers (Re_2).

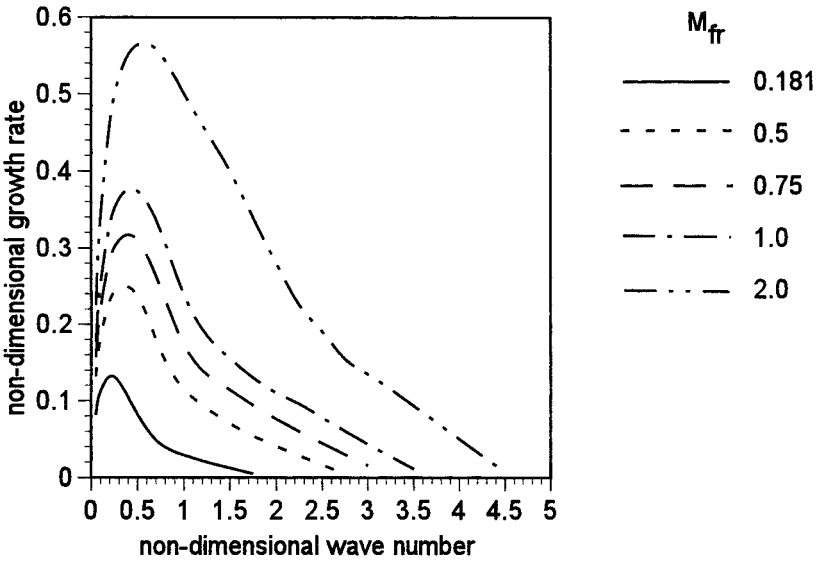

Figure 7. Dimensionless temporal growth rate as a function of non-dimensional wavenumber for $\mathrm{Re}_1 = 340$, $\mathrm{Re}_2 = 460$, $\mathrm{We} = 9.7$, $l = 1.4$, $V_{21} = 12.5$ and several momentum flux ratios (M_{fr}).

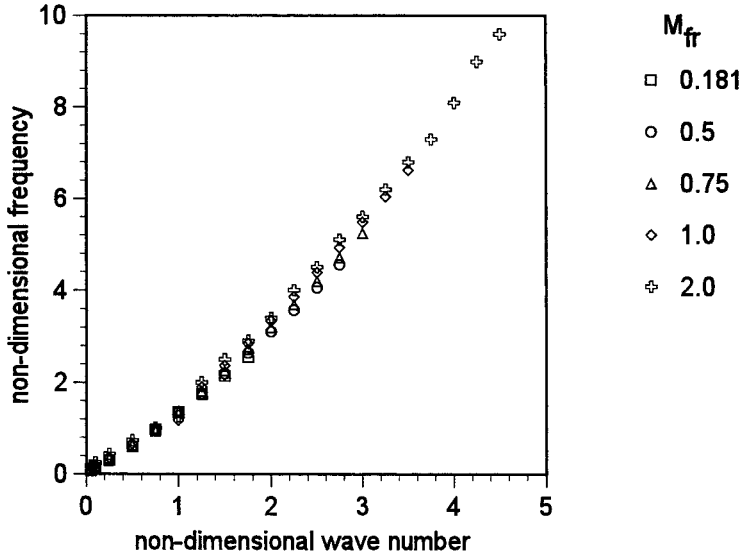

Figure 8. Dimensionless temporal frequency as a function of non-dimensional wavenumber for Re_1, Re_2, We, l, V_{21} as in Figure 5, and several momentum flux ratios (M_{fr}).

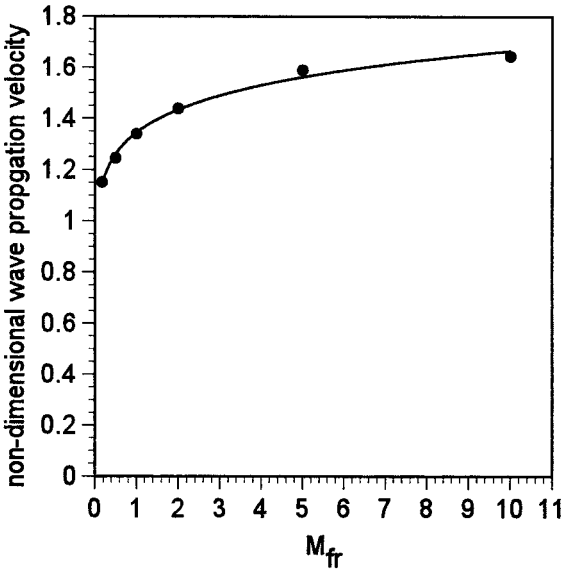

Figure 9. Dimensionless wave propagation speed as a function of M_{fr}.

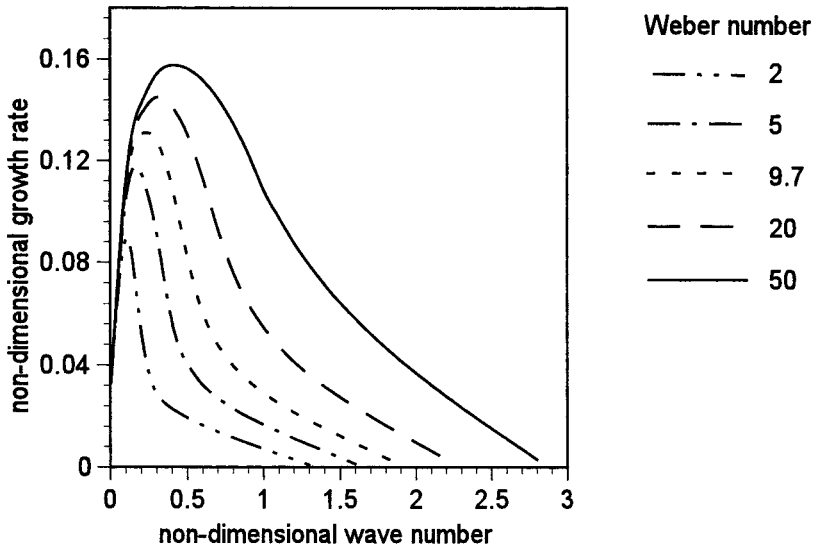

Figure 10. Dimensionless temporal growth rate as a function of non-dimensional wavenumber for $\mathrm{Re}_1 = 340$, $\mathrm{Re}_2 = 460$, $M_{\mathrm{fr}} = 0.181$, $l = 1.4$, $V_{21} = 12.5$ and several Weber numbers (We).

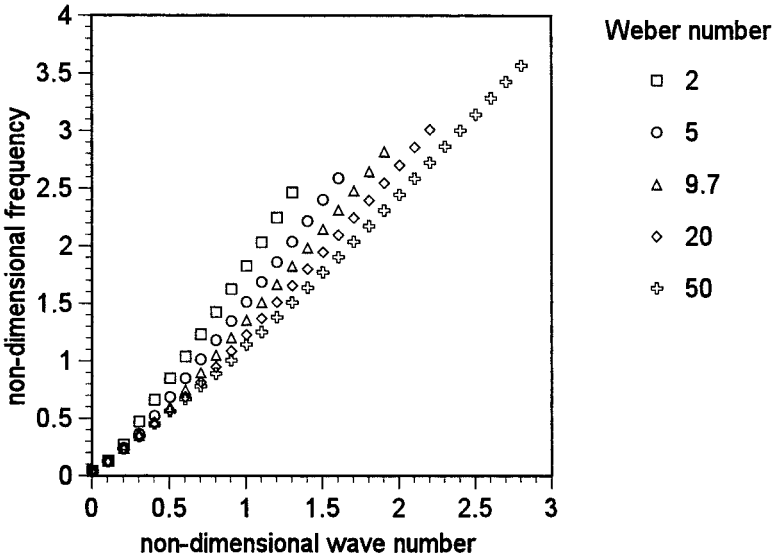

Figure 11. Dimensionless temporal frequency as a function of non-dimensional wavenumber for the same values of Re_1, Re_2, M_{fr}, l, V_{21} as in Figure 8, and several Weber numbers (We).

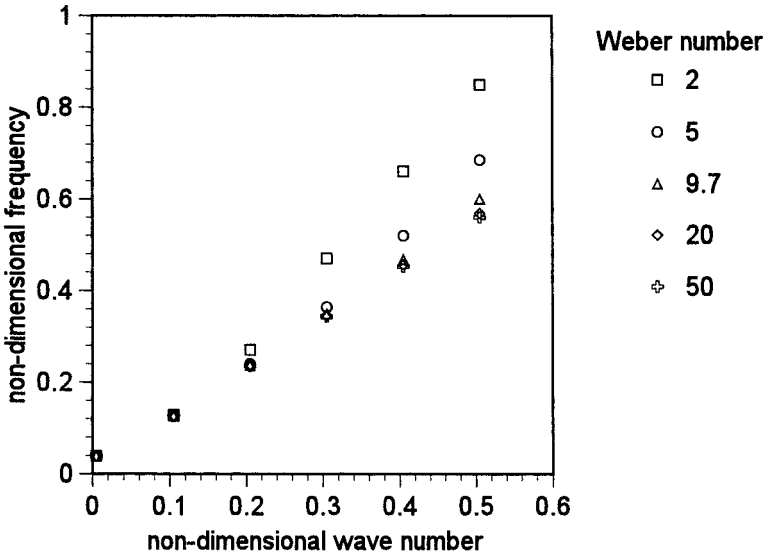

Figure 12. Blowup of Figure 11 for small values of the non-dimensional wavenumbers.

to instabilities as We is increased because the surface tension has a minor effect on small curvatures. Figures 11 and 12 illustrate the behavior of the wave propagation speed. A change of slope in the dimensionless frequency (and thus, in the wave propagation speed) can be again observed at the inflection point of the growth rate-wavenumber curve. For wavenumbers below the inflection point (i.e., for small wavenumbers), the wave speed is independent of the We number and is basically equal to the liquid speed (for small M_{fr} numbers). For wavenumbers above the inflection point (i.e., for large wavenumbers), an increase of the wave speed can be noticed, which decreases with increasing Weber number. In this case, the behavior of the interface, significant for larger values of the surface tension, yields an increment of the wave speed to values almost twice that of the liquid velocity; this trend is also present for large wavelength oscillations.

4.2. Variation of dimensional parameters

In the previous subsection an analysis varying a single dimensionless group and keeping the remaining ones constant has been performed. However, in most experimental situations, only the physical variables, such as velocity, pressure or geometrical parameters, can be directly controlled whereas the fluid properties are usually kept constant.

For this reason, an analysis has also been performed for constant properties of the two fluids as well as constant liquid and gas velocities, $\bar{U}_1$ and $U_{2\infty}$, respectively; the parameter δ, representative of the gas boundary layer thickness, has then been varied, while the liquid sheet thickness, h, has been kept constant. Re_1, M_{fr},

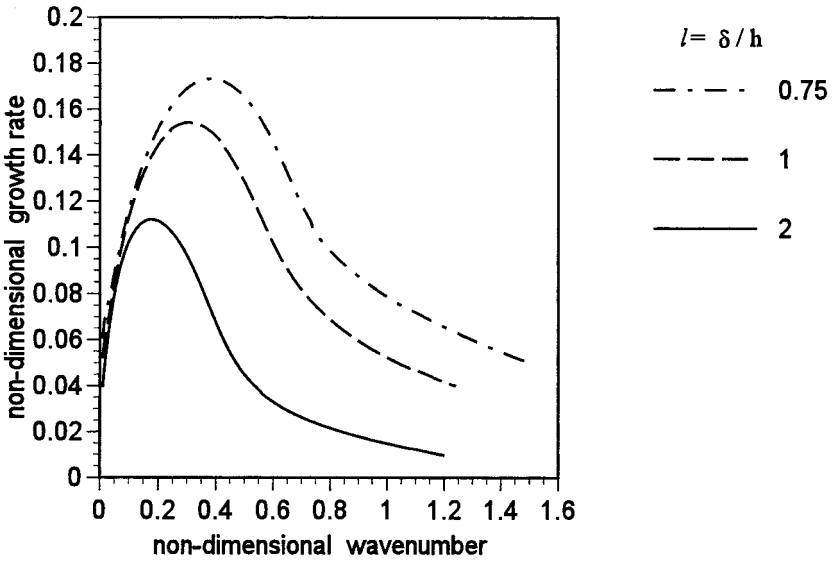

Figure 13. Dimensionless temporal growth rate as a function of non-dimensional wavenumber for $\mathrm{Re}_1 = 340$, $\mathrm{Re}_2 = 0.83l\,\mathrm{Re}_1$, $M_{\mathrm{fr}} = 0.181$, We $= 9.7$, $V_{21} = 12.5$ and several ratios of the boundary layer thickness to liquid half-width ($l = \delta/h$).

We and V_{21} are, therefore, constant and Re_2 is linearly dependent of $l = \delta/h$. ($\mathrm{Re}_2 \approx 0.83l\mathrm{Re}_1$). Figure 13 displays the influence of l upon the temporal growth rate as a function of the wavenumber. Increasing the thickness ratio, l, has a stabilizing effect on the liquid sheet oscillation, specially on the growth rate value. For a constant h, larger l implies a thicker boundary layer; as $\bar{U}_1$ is constant, a thicker boundary layer (large l) contains less vorticity than a thinner one (small l). As the liquid sheet deforms, the more intense the vorticity patterns (small l) in the basic flow, the stronger the induced destabilizing pressure fields. This behavior has been unveiled by López-Pagés [23] through numerical simulation of a two-dimensional liquid sheet with gaseous coflows.

The boundary layer thickness is then one of the key physical parameters governing this process. Therefore, the boundary layer and its associated viscous effects cannot be ignored if the instability of sheets in air-assisted situations is to be correctly predicted.

Figure 13 can also be used to discuss the effect of liquid sheet thickness variation. Reducing h while maintaining δ constant has the same effect as increasing l through a boundary layer thickness increment. Thinner liquid sheets seem to be more stable for all wavelengths, but specially for the small wavenumber range where the maximum growth rate takes place. However, this behavior is not observed experimentally. In this respect, it is worth pointing out that keeping constant the properties of the two fluids, $\bar{U}_1$, $U_{2\infty}$ and δ, and varying the liquid sheet thickness, h, will imply simultaneous variations in Re_1, We and l; a reduction in h

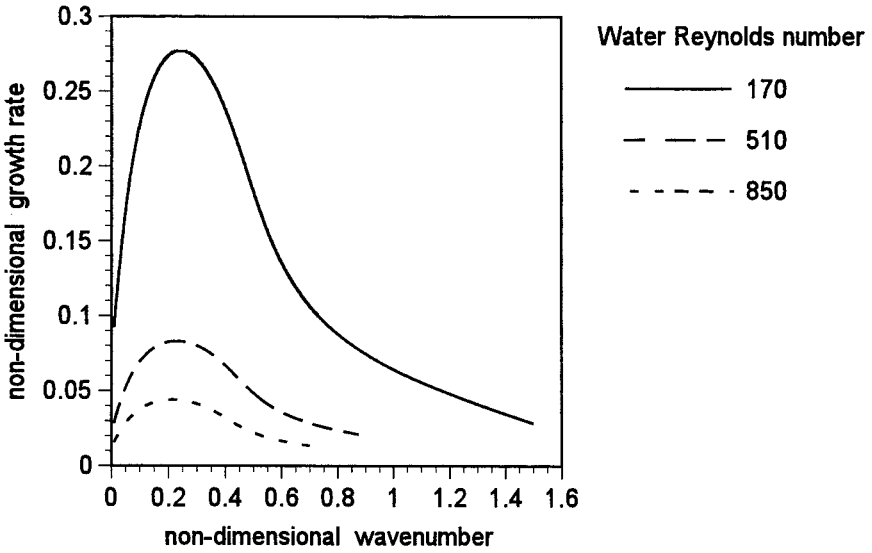

Figure 14. Dimensionless temporal growth rate as a function of non-dimensional wavenumber for $\mathrm{Re}_1 = 460$, $U_{2\infty} = 25$ m/s, $l = 1.4$, physical liquid properties corresponding to the water, and several liquid Reynolds numbers. For $\bar{U}_1 = 1$ m/s; $\mathrm{Re}_1 = 170$, $M_{\mathrm{fr}} = 0.73$, We $= 2.43$ and $V_{21} = 25$; for $\bar{U}_1 = 3$ m/s; $\mathrm{Re}_1 = 510$, $M_{\mathrm{fr}} = 0.08$, We $= 21.88$ and $V_{21} = 8.33$; and for $\bar{U}_1 = 5$ m/s; $\mathrm{Re}_1 = 850$, $M_{\mathrm{fr}} = 0.03$, We $= 60.76$ and $V_{21} = 5$.

simultaneously leads to a combination of stabilizing effects due to the increment of l and to the reduction of Re_1 and We.

Figures 14 and 15 are plots of the growth rate as a function of the wavenumber for several $\bar{U}_1$ and $U_{2\infty}$, respectively; maintaining all the remaining fluid properties and thicknesses constant. These are typical experimental results (see, for example, [1]) when liquid and air velocities are easily controlled. All one can say in connection with Figure 14 is that the combined action of de-stabilizing effects, through the increments of Re_1 and We, and stabilizing effects, through the reduction of M_{fr}, yield an overall stabilizing result, manifested mainly in significantly lower growth rates. Similarly, Figure 15 illustrates that, for Re_1, We and l constants, the de-stabilizing action of an increment in the M_{fr} overcomes the stabilizing effects of a growth in the Re_2. In both instances, the controlling dimensionless group seems to be the momentum flux ratio.

Changing only the liquid density, ρ_1, simultaneously changes the values of Re_1, M_{fr} and We. Figure 16 indicates that the overall effect of increasing ρ_1 is a stabilization of the liquid sheet with a significant reduction in the growth rate for small wavenumbers and comparable growth rates for asymptotically large wavenumbers. Again, the de-stabilizing action of the increments of Re_1 and We is overcome by the stabilizing effects of the reduction in the M_{fr}. Figure 17 clearly shows that liquid density variations lead to significant changes in the wave propagation speed.

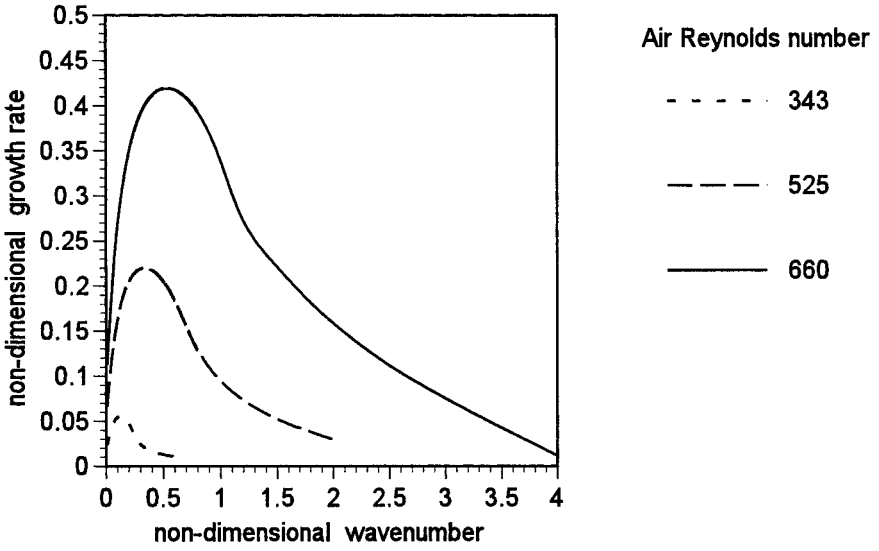

Figure 15. Dimensionless temporal growth rate as a function of non-dimensional wavenumber for $U_1 = 2$ m/s, $\mathrm{Re}_1 = 340$, We $= 9.7$, $l = 1.4$, physical gas properties corresponding to air and liquid corresponding to water. For $U_{2\infty} = 15$ m/s; $\mathrm{Re}_2 = 343$, $M_{\mathrm{fr}} = 0.07$ and $V_{21} = 7.5$; for $U_{2\infty} = 35$ m/s; $\mathrm{Re}_2 = 525$, $M_{\mathrm{fr}} = 0.35$ and $V_{21} = 17.5$; and for $U_{2\infty} = 55$ m/s; $\mathrm{Re}_2 = 660$, $M_{\mathrm{fr}} = 0.88$ and $V_{21} = 27.5$.

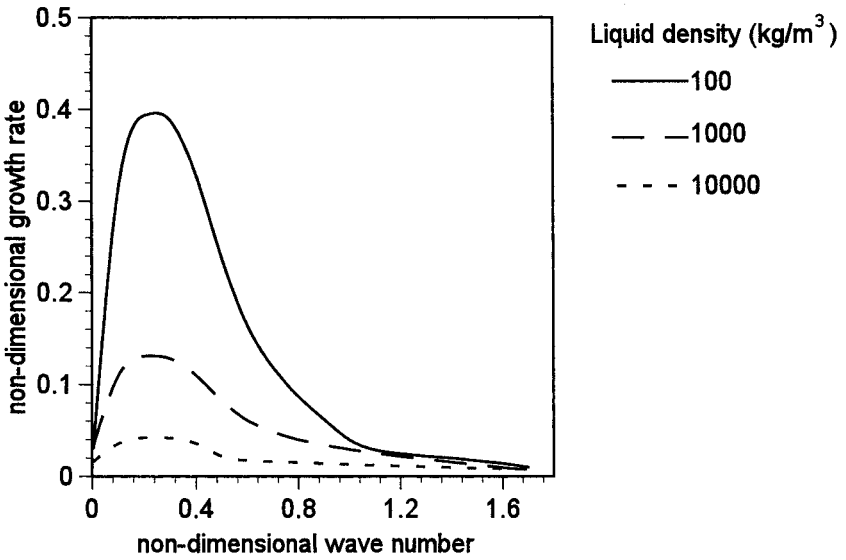

Figure 16. Dimensionless temporal growth rate as a function of non-dimensional wavenumber for $\bar{U}_1 = 2$ m/s, $U_{2\infty} = 25$ m/s, $\mathrm{Re}_2 = 460$, $V_{21} = 12.5$, $l = 1.4$, and several liquid densities. For $\rho_1 = 100$ kg/m^3, $\mathrm{Re}_1 = 34$, $M_{\mathrm{fr}} = 1.81$ and We $= 0.97$; for $\rho_1 = 1000$ kg/m^3, $\mathrm{Re}_1 = 340$, $M_{\mathrm{fr}} = 0.181$ and We $= 9.72$; and for $\rho_1 = 10000$ kg/m^3, $\mathrm{Re}_1 = 3400$, $M_{\mathrm{fr}} = 0.018$ and We $= 97.2$.

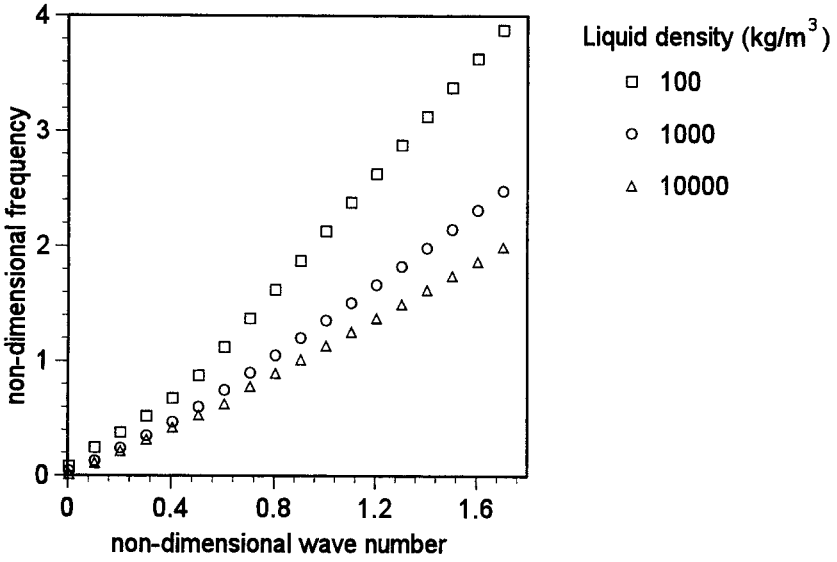

Figure 17. Dimensionless temporal frequency as a function of non-dimensional wavenumber for the same conditions as in Figure 14.

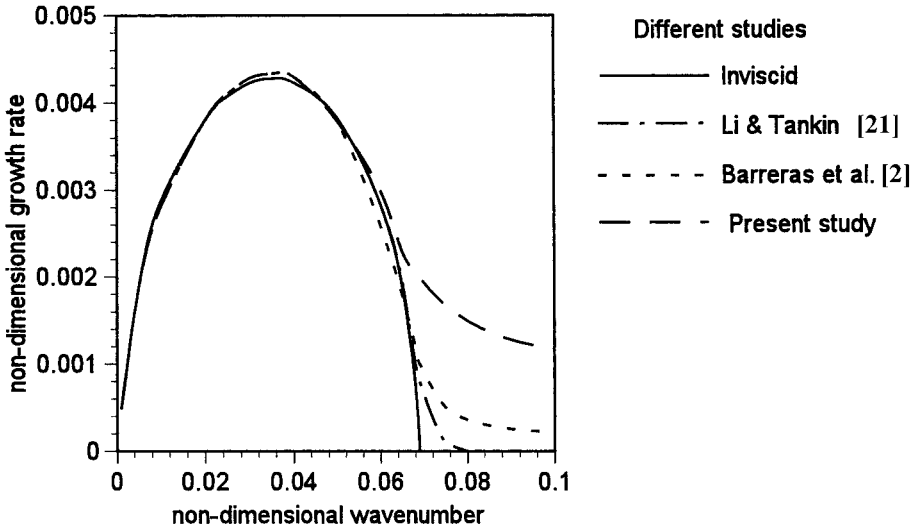

Figure 18. Comparison of temporal growth rate as a function of non-dimensional wavenumber resulting from the various existing studies and the present one. The parameters considered in this figure are $U_1 = 5$ m/s ($\mathrm{Re}_1 = 850$), $U_{2\infty} = 10$ m/s ($\mathrm{Re}_2 = 330$) and for a water/air system.

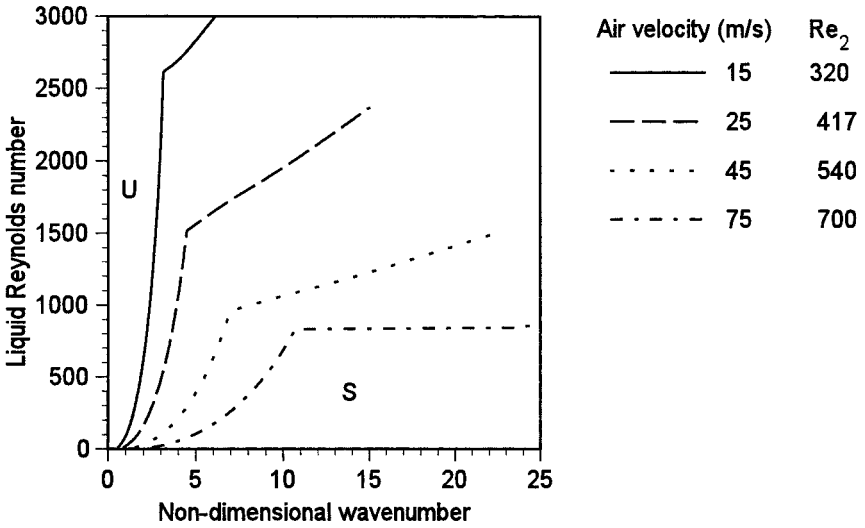

Figure 19. Neutral stability curves for various gas velocities and $\bar{U}_1 = 1$ m/s, $\rho_1 = 998$ kg/m^3, $\rho_2 = 1.2$ kg/m^3, $\mu_2 = 0.018 \cdot 10^{-3}$ Pa-s, $\sigma = 0.072$ N/m and $h = 0.175$ mm. The gas boundary layer thickness is, respectively, 0.32, 0.25, 0.18 and 0.14 mm (U unstable region and S stable region).

Finally, for the same values of the physical parameters, Figure 18 compares the results of previous studies (inviscid, [22] and inviscid basic flow/viscous perturbation) with those of the present study. The inviscid and the Li and Tankin predictions perfectly coincide. This is so because the $M_{\text{fr}} = 0.004$ is very small. For the values used in this comparison the discrepancies seem to be limited to large wavenumbers beyond the region of maximum growth rates. In general, the effects of the boundary layer cause a reduction in the maximum growth rate and the corresponding wavenumber.

4.3. Neutral stability curves

Figures 19 and 20 show neutral stability curves (Re_1 *versus* k) for various air velocities. The properties of air have been taken for the gas, whose boundary layer thickness has been changed accordingly to the air speed. The liquid Reynolds number has been obtained keeping the water properties constant with a liquid speed of 1 m/s, but varying the liquid viscosity. The abscissa of the plots has been limited to a dimensionless wavenumber of 22, which for a sheet thickness of 350 μm corresponds to a fairly small wavelength of 100 μm; this wavelength is much shorter than the experimental value observed under these conditions [1].

Each curve in Figure 19 separates the zones of stability, (to the right of the curves and marked as S) and instability (to the left of the curves and marked as U). Figure 20 has been obtained at a fixed water velocity of 1 m/s and air velocity of

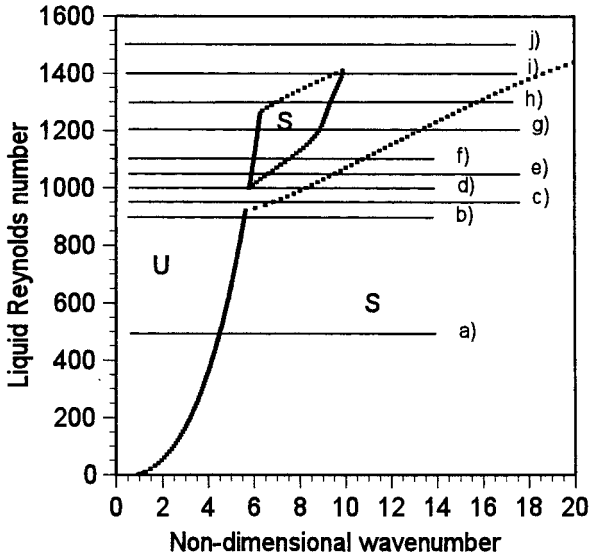

Figure 20. Neutral stability curves for an air speed of 45 m/s ($\delta = 0.25$ mm). The remaining parameters are the same as in Figure 19 (U unstable region and S stable region).

45 m/s. The only difference with the data of Figure 19 is that the boundary layer thickness for that air speed (0.18 mm) has been changed to 0.25 mm; the influence of δ/h and the viscous effects are thus apparent. It can be observed how a slight variation of the δ/h ratio dramatically change the curves of neutral stability. In this case, even a stability island, which was not present before, is apparent.

Figure 21 depicts the evolution of the non-dimensional growth rates along the cuts displayed in Figure 20. The changes in slope of the neutral stability curves depend on different eigenvalues emerging and disappearing.

4.4. STREAMFUNCTIONS

Figure 22 shows the real part of a typical streamfunction at the wavenumber of maximum growth rate. The imaginary part is negligible. It can be noted that the vertical velocity perturbation is basically constant and decreases in the gas boundary layer region to match the decaying analytical solution of the outer part. A smooth tiny kink can be observed at the interface $y = 1$ in the gas region. This maximum can be explained by the continuity of the streamfunction and its derivative across the gas/liquid interface. Since the slope of the streamfunction is positive in the liquid region and at the same time it has to vanish very far from the centerline, there must exist and inflection point in the gas boundary layer. Therefore, although the present computation cannot give reliably the magnitude of the kink, its presence is physically plausible. Similar behaviour was found in [21]. The horizontal velocity perturbations are basically zero in the liquid domain, whereas they are large in

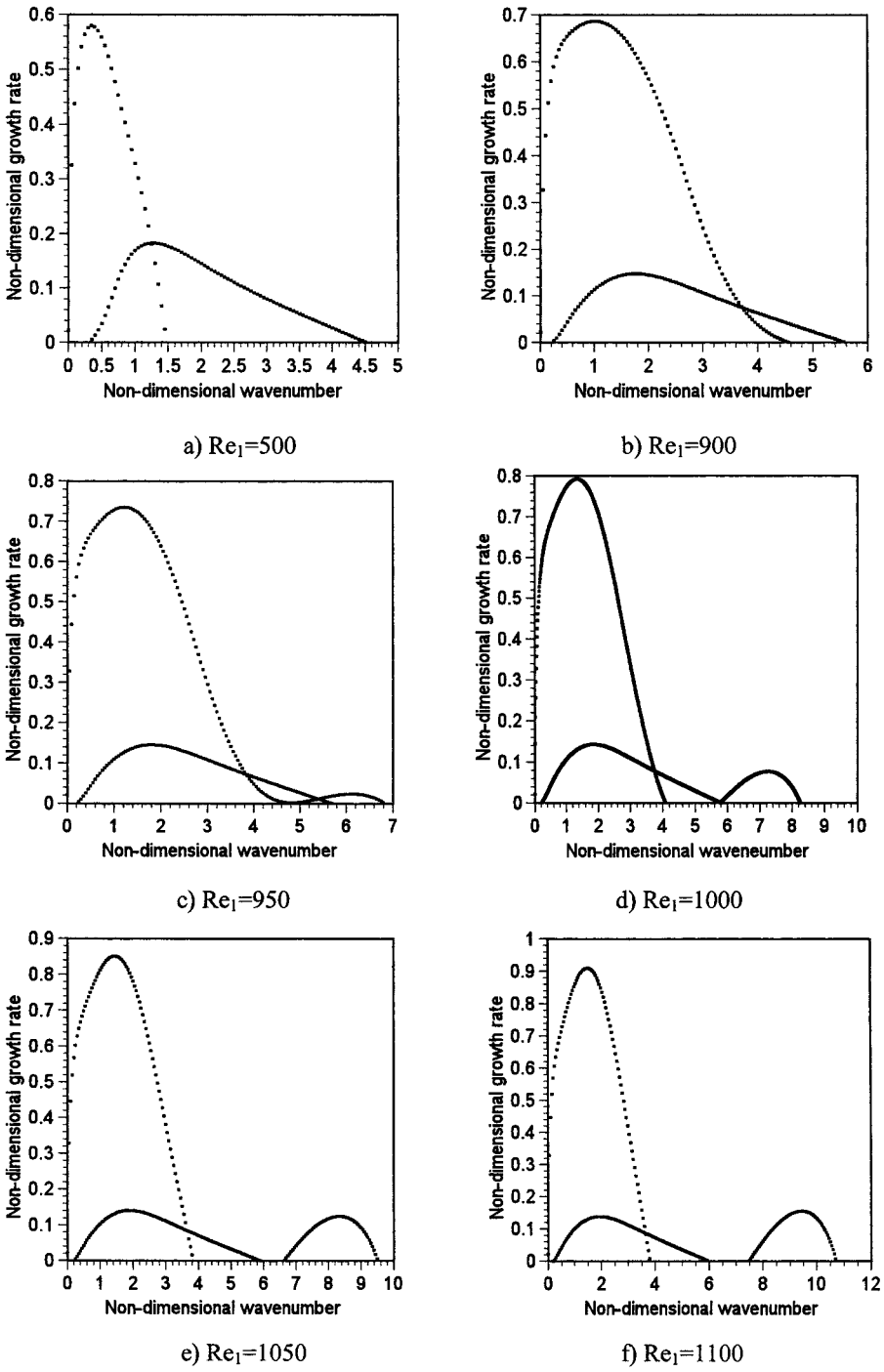

Figure 21. Dimensionless temporal growth rate as a function of non-dimensional wavenumber for the Reynolds numbers shown in Figure 20.

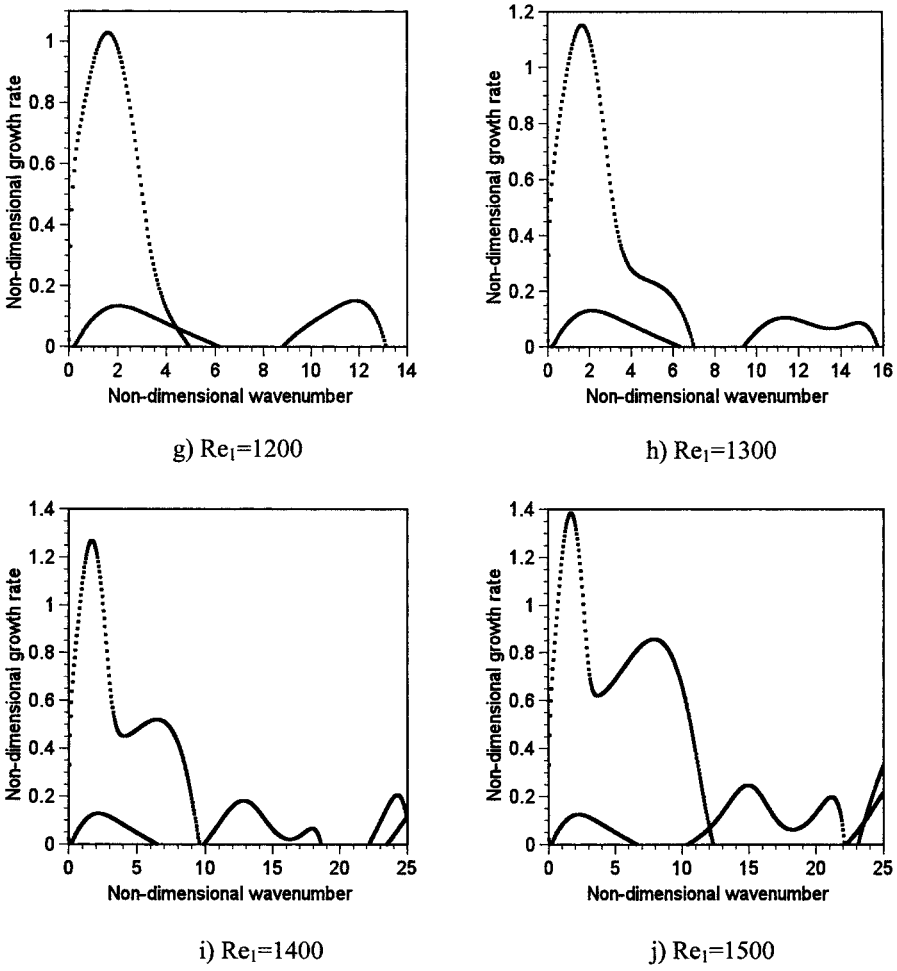

Figure 21. Continued.

the gas region, specially, at the kink nearby the interface. Therefore, it might be concluded that the horizontal instability is mainly engendered at the interface and resides in the gas boundary layer.

5. Conclusions

The viscous linear temporal instability of a plane liquid sheet between two semi-infinite gaseous coflows has been studied. This configuration is representative of air-assisted atomizers. It is the first time in which both fluids have been treated as viscous. The complete Orr–Sommerfeld equations and boundary conditions have been formulated and numerically integrated. Only the antisymmetric or sinuous mode has been investigated, since this is the only one experimentally observed.

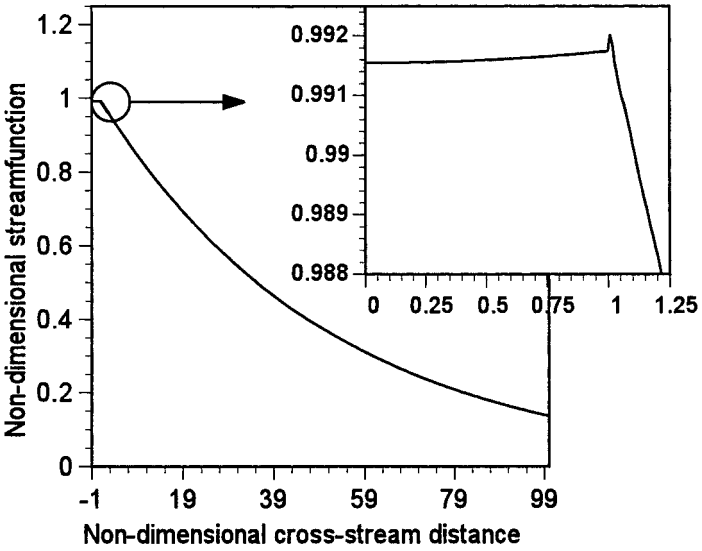

Figure 22. Non-dimensional streamfunction (modulus) *versus* non-dimensional cross-stream distance for $\bar{U}_1 = 1$ m/s ($\mathrm{Re}_1 = 170$) and $U_{2\infty} = 15$ m/s ($\mathrm{Re}_2 = 343$). Physical properties for the gas and the liquid correspond to those of air and water respectively ($\rho_1 = 998$ kg/m^3, $\mu_1 = 0.89 \cdot 10^{-3}$ Pa-s, $\rho_2 = 1.2$ kg/m^3, $\mu_2 = 0.018 \cdot 10^{-3}$ Pa-s, $\sigma = 0.072$ N/m), and a non-dimensional wavenumber value of 0.02 corresponding to the point for maximum growth rate for $\delta = 0.32$ mm and $h = 0.175$ mm.

Six relevant dimensionless groups have emerged in this analysis. Apart from the liquid and gas Reynolds numbers, the Weber number and the gas/liquid velocity ratio, two previously ignored dimensionless numbers, namely, the momentum flux ratio and the gas boundary layer thickness to the liquid sheet thickness relation, l, have been observed to have a rather significant effect on the sheet instability.

A detailed parametric analysis has been conducted, first varying individually Re_1, Re_2, M_{fr}, We, and then changing several physical quantities (l, ρ_1, $\bar{U}_1$, $U_{2\infty}$). Neutral stability curves have also been presented. As a summary, increasing the momentum flux ratio has a de-stabilizing effect upon the liquid sheet as the dynamic pressure of the gas increases compared to that of the liquid. Increasing l leads to a more stable behavior of the sheet. The boundary layer thickness has demonstrated to have a large influence upon the neutral stability curve. Therefore, the viscous effects are of paramount importance to predict this instability, which governs the mechanics of twin-fluid atomization processes.

References

1. Barreras, F., Experimental study of the break-up and atomization of a liquid sheet. Ph.D. Dissertation, University of Zaragoza (1998) [in Spanish].
2. Barreras, F., Lozano, A. and Dopazo, C., Linear instability analysis of the viscous longitudinal perturbation on an air-blasted liquid sheet. *Atom. & Spray* **11**(2) (2001) 139–154.

3. Benjamin, T.B., Shearing flow over a wavy boundary. *J. Fluid Mech.* **6** (1959) 161–205.
4. Bertolotti, F.P., Herbert, Th. and Spalart, P.R., Linear and nonlinear stability of the Blasius boundary layer. *J. of Fluid Mech.* **242** (1992) 441–474.
5. Blennerhassett, P.J., On the generation waves by winds. *Philos. Trans. Roy. Soc. London A* **298** (1980) 451–494.
6. Cousin, J. and Dumouchel, C., Effect of viscosity on the linear instability of a flat liquid sheet. *Atom. & Spray* **6**(5) (1996) 563–576.
7. Crapper, G.D., Dombrowski, N. and Pyott, G., Large amplitude Kelvin–Helmholtz waves on thin liquids sheets. *Proc. Roy. Soc. London A* **342** (1975) 209–224.
8. Crapper, G.D., Dombrowski, N. and Jepson, W.P., Waves on thin sheets of non-newtonian liquids. *Proc. Roy. Soc. London A* **342** (1975) 225–236.
9. Criminale, W.O., Jackson, T.L., Lasseigne, D.G. and Joslin, R.D., Perturbation dynamics in viscous channel flows. *J. Fluid Mech.* **339** (1997) 55–75.
10. Dombrowski, N., Hasson, D. and Ward, D.E., Some aspects of liquid flow through fan spray nozzles. *Chem. Engrg. Sci.* **12** (1960) 35–50.
11. Dombrowski, N. and Johns, W.R., The aerodynamic instability and disintegration of viscous liquid sheets. *Chem. Engrg. Sci.* **18** (1963) 203–214.
12. Fraser, R.P., Dombrowski, N. and Routley, J.H., The atomization of a liquid sheet by an impinging air stream. *Chem. Engrg. Sci.* **18** (1963) 339–353.
13. Gaster, M., On the effects of boundary-layer growth on flow stability. *J. Fluid Mech.* **66** (1974) 465–480.
14. Gottlieb, D. and Orszag, S.A., *Numerical Analysis of Spectral Methods: Theory and Applications*. CBMS-NSF Regional Conference Series in Applied Mathematics, Vol. 26, SIAM, Philadelphia, PA (1977).
15. Hagerty, W.W. and Shea, J.F., A study of the stability of plane fluid sheets. *J. Appl. Mech.* **22** (1955) 509–514.
16. Huerre, P., Shear flow instabilities: Amplifiers versus oscillators. RTD/AGARD Course, Madrid Polytechnic University, Madrid (1999).
17. Ibrahim, E.A., Spatial instability of a viscous liquid sheets. AIAA Paper 94-0562 (1994) pp. 1–7.
18. Ibrahim, E.A., Effects of compressibility on the instability of liquid sheets. AIAA Paper 95-2431 (1995).
19. Ibrahim, E.A. and Akpan, E.T., Three-dimensional instability of viscous liquid sheets. *Atom. & Sprays* **6** (1996) 649–665.
20. LAPACK, University of Tennessee, University of California Berkeley, NAG Ltd., Courant Institute, Argonne National Lab, and Rice University (1999).
21. Lin, S.P., Lian, Z.W. and Creighton, B.J., Absolute and convective instability of a liquid sheet. *J. Fluid Mech.* **220** (1990) 673–689.
22. Li, X. and Tankin, R.S., On the temporal instability of a two-dimensional viscous liquid sheet. *J. Fluid Mech.* **226** (1991) 425–443.
23. López-Pagés, E., Simulación numérica de inestabilidades en interfases líquido-gas. Ph.D. Dissertation, Centro Politécnico Superior, Universidad de Zaragoza (2000).
24. Lozano, A., Barreras, F., Hauke, G. and Dopazo, C., Longitudinal instabilities in an air-blasted liquid sheet. *J. Fluid Mech.* **437** (2001) 143–173.
25. Mansour, A. and Chigier, N., Dynamic behavior of liquid sheets. *Phys. Fluids A* **2**(5) (1991) 2971–2980.
26. Miesen, R. and Boërsma, B.J., Hydrodynamic stability of a sheared liquid film. *J. Fluid Mech.* **301** (1995) 175–202.
27. Miles, J.W., On the generation of surface waves by shear flows, Part 4. *J. Fluid Mech.* **13** (1962) 433–488.

28. Orszag, S.A., Accurate solution of the Orr–Sommerfeld stability equation. *J. Fluid Mech.* **50** (1971) 689–703.
29. Rangel, R.H. and Sirignano, W.A., The linear and non-linear shear instability of a fluid sheet. *Phys. Fluids A* **3**(10) (1991) 2392–2400.
30. Renardy, Y., Viscosity and density stratification in vertical Poiseuille flow. *Phys. Fluids* **30** (1987) 1638–1648.
31. Savart, F., Mémoire sur le choc d'une veine liquide lancée contre un plan circulaire. *Ann. de Chim.* **54** (1833) 56–87.
32. Smith, M.K., The mechanism for the long-wave instability in thin liquid films. *J. Fluid Mech.* **217** (1990) 469–485.
33. Smith, M. and Davis, S., The instability of sheared liquid layers. *J. Fluid Mech.* **121** (1982) 187–206.
34. Squire, H.B., Investigation of the instability of moving liquid film. *British J. Appl. Phys.* **4** (1953) 167–169.
35. Taylor, G.I., The dynamics of thin sheets of fluid. I. Water bells. *Proc. Roy. Soc. London A* **253** (1959) 280–296.
36. Taylor, G.I., The dynamics of thin sheets of fluid. II. Waves on fluid sheets. *Proc. Roy. Soc. London A* **253** (1959) 296–312.
37. Teng, C.H., Lin, S.P. and Chen, J.N., Absolute and convective instability of a viscous liquid curtain in a viscous gas. *J. Fluid Mech.* **332** (1997) 105–120.
38. Tilley, B.S., Davis, S.H. and Bankoff, S.G, Linear stability theory of two-layer flow in an inclined channel. *Phys. Fluids* **6** (1994) 3906–3922.
39. Yang, H.Q., Interfacial instability between a liquid film and the surrounding compressible gas. AIAA Paper 92-0461 (1992).
40. Yiantsios, S.G. and Higgins, B.G., Linear stability of plane Poiseuille flows of two superposed fluids. *Phys. Fluids* **31** (1998) 3225–3238.
41. Yih, C.S., Waves formation on a liquid layer for de-icing airplane wings. *J. Fluid Mech.* **212** (1990) 41–53.
42. York, J.L., Stubbs, H.E. and Tek, M.R., The mechanisms of disintegration of liquid sheets. *Trans. ASME* October (1953) 1279–1286.